Environmental Science
Water Research & Technology

Understanding Resistances in Capacitive Deionization Devices

Journal:	*Environmental Science: Water Research & Technology*
Manuscript ID	EW-ART-02-2020-000169.R1
Article Type:	Paper

Water Impact Statement

The desalination characteristics of capacitive desalination are strongly influenced by the resistive components of the system. Here we provide a comprehensive practical overview of a CDI cell's resistive components both experimentally and theoretically. In doing so, we detail new methods for separating the impact of contact vs. electrode effects as well as provide an explanation of poorly understood impedance features.

Understanding Resistances in Capacitive Deionization Devices

Helen A. Kuo,† Ashwin Ramachandran,‡ Diego I. Oyarzun,† Erica C. Clevenger,† Juan G. Santiago,¶ Michael Stadermann,† Patrick G. Campbell,† and Steven A. Hawks*,†

†*Lawrence Livermore National Laboratory, 7000 East Avenue, Livermore, CA 94550, United States*

‡*Department of Aeronautics & Astronautics, Stanford University, Stanford, CA 94305, United States*

¶*Department of Mechanical Engineering, Stanford University, Stanford, CA 94305, United States*

E-mail: hawks3@llnl.gov

Abstract

The desalination characteristics of capacitive deionization (CDI) are significantly impacted by the cell resistance. Here we apply electrochemical impedance spectroscopy (EIS) to analyze the resistive properties of a CDI device, which include EIS measurements on a complete assembled cell (in two wire mode) and EIS measurements with additional contacts to decouple electrode/electrolyte and contact impedances (four wire mode). These measurements shed light on the interface between current collector and electrode and the internal capacitive and resistive elements of the cell. With two-wire and four-wire EIS measurements, we find that the often-observed high-frequency arc(s) in the impedance spectra can be due to contact effects and/or an internal ionic-transfer resistance that is locally in parallel with macropore wall capacitance. In some cases, the two associated arcs

in the Nyquist plot are overlapping and present simultaneously, making their identification in the EIS spectra difficult unless both two-wire and four-wire measurements are made. Despite causing a large high-frequency arc in the Nyquist plot, we find that the apparent internal ionic-transfer resistance is negligible compared to the resistances of the electrode, separator, and external electronic components. An investigation of the contact impedance between the electrode and current collector reveals a parallel *RC* arc that can grow over time if an improper material is used (e.g., titanium). In our system, the electrode ionic resistance dominates the total Ohmic power dissipation, which has implications for scale-up of CDI systems and future improvements of cell design.

Introduction

Capacitive deionization (CDI) is a technique for water desalination that could be economically viable for selectively removing ions or treating low salinity water (e.g. <20 mM NaCl or 1200 ppm equivalent salinity).[1–7] In typical CDI operation, a voltage is applied to a pair of porous carbon electrodes and ions are pulled from the water to form electrical double layers (EDLs) within the pores of the electrodes. Subsequently the electrodes are discharged in order to release the ions into a concentrate stream and prepare the device for another desalination phase. Two of the main energy drains are resistive losses and parasitic Faradaic reactions. Faradaic reactions can be managed by limiting the maximum voltage and the time spent at elevated voltage, while resistive losses can be reduced by applying lower-magnitude current densities and decreasing the system resistances.[8,9] In high-current conditions, which are necessary for high-throughput operation, reducing resistive losses is especially important given that *RC* and transmission line-type charging physics underlie the charging dynamics.[10,11] Since the system resistances influence both salt

removal rate and energy consumption, it is an especially important characteristic to understand and minimize.

In order to reduce resistive losses, the system resistances due to various components must be isolated, understood, and quantified. CDI technology is similar to that of supercapacitors, and several electrode impedance models are common to both technologies.[12–20] Similarly, a large body of work has focused on the development of new materials for CDI electrodes,[21,22] much of which includes resistance characterization.[23–38] However, materials-focused studies (particularly ex situ measurements of electrode material) often do not provide an in-depth analysis as to what mechanisms underlie the different features observed in the impedance spectra. Additionally, many resistance/impedance studies do not consider all resistive components of the system, making the overall contribution of a given component unclear. For example, the lack of a clear picture of the various resistances has led to recent controversy regarding predictions of CDI performance with simple resistive models,[39–42] and this prompts a deeper look into the resistances of CDI cells.

A primary example of poorly understood resistance characteristics in porous electrode systems is the anomalous arc in the Nyquist plot at high frequencies (Fig. 1 (d)), indicative of parallel capacitive and resistive behavior. There is no consensus among the models and experimental studies as to what causes this high-frequency arc, which has been attributed to ion transport,[19,24] electrode geometry,[13,20,33] electrode-electrolyte interfaces,[32] interfaces among activated carbon particles,[25–27] interfaces between current collectors and electrode material,[28,43] surface chemistry of the electrode,[44] an unexplained transfer resistance,[30,31] or some combination of these effects.[37,38,45] This is most concerning because a simple parallel *RC* interpretation of the feature suggests that it is a significant hindrance to charging rate capability and a major contributor to the Ohmic power dissipation. The presence of such

unknown components makes it difficult to assess the relative importance of the various resistances to the Ohmic power dissipation and charging rate capability.

Apart from the unclear cause(s) of these arc shapes in Nyquist plots, there are other poorly understood resistances in a full CDI cell. Although there have been several studies of supercapacitor device resistances,[12,24,46,47] the relative contribution of resistances to overall impedance in a CDI cell are very different as the CDI electrolyte concentration is typically about two orders of magnitude lower than that of supercapacitors. There are some studies, however, that have focused on resistances in full CDI cells. For example, Qu *et al.*[48] found that, in their devices, the impedance of the contact between the current collector and the electrode was the largest contributor to the overall Ohmic dissipation and was responsible for the anomalous high-frequency impedance arc.[48] They further found that the contribution of contact resistance can be reduced with pressure or through the use of a conductive silver

epoxy, similar to previous results with Li-ion electrode current collector connections.[49,50] Dykstra *et al.*[51] analyzed resistances in membrane CDI (MCDI) cells throughout a desalination cycle using a combined modified-Donnan and one-dimensional (1D) transport model. Their results originally showed ionic resistances in the separator channel of the cell to be the most significant, though their definition of ionic resistances in the electrodes was later refined and the contribution of electrode ionic resistances was shown to be more comparable to the separator ionic resistances.[51,52] Van Limpt investigated many aspects of CDI cell resistances and found that, at typical CDI electrolyte concentrations, the electrode ionic resistances were the main contributor to the Ohmic power dissipation of the cell. Notably, Van Limpt ascribed the anomalous high-frequency arc in the impedance spectrum to a temperature dependent charge-transfer reaction but admitted that the mechanism behind the charge-transfer process was unclear.[53]

Although not initially employed at CDI-relevant concentrations, a model applicable to CDI cells was developed by Suss *et al.*[14] to describe the impedance of hierarchically porous electrodes. They described a network of mesoporous transport pores with smaller storage pores along the walls using a nested transmission line model. This model allows for the extraction of the resistance and capacitance of transport and storage pores from an impedance spectrum. Suss *et al.*[14] accounted for the anomalous high-frequency impedance arc by including a resistance to enter the storage pores, termed R_{sub-nm}. It is noteworthy that the Suss *et al.*[14] model embeds R_{sub-nm} as a nested transmission line element rather than placing it in parallel to the transmission line as in most other commonly applied equivalent circuits.[24,30,31]

Here we extend the work of Qu *et al.*,[48] Van Limpt,[53] Suss *et al.*[14] and Dykstra *et al.*[51] in examining the resistances of an entire CDI cell. We present and verify a breakdown of CDI cell resistances which can be easily extracted from an EIS measurement without complicated fitting. By examining each component of the resistance breakdown, along with the corresponding impedance spectrum features, we resolve which resistances are most important for our system and explore the implications for cell design and scaleup. By comparing impedance measurements at different electrode thicknesses, electrolyte concentrations, and in two- and four-wire measurement modes, we clearly separate the effects of the current collector contact from other electrode and cell impedance effects. Using this technique, we find that there are in fact two different contributors to the observed high-frequency impedance arcs, one of which is due to contact effects as seen by Qu *et al.*[48] and the other due to the so-called internal ionic-transfer resistance as alluded to in Suss *et al.*[14] By applying a modified version of the model developed by Suss *et al.*,[14] we find that the internal ionic transfer resistance, although responsible for a large arc in the impedance spectrum, is in fact not a significant contributor to the overall Ohmic

dissipation. Instead, for our system, we find that the ionic resistances of the electrolyte within the electrodes is the most significant contributor to Ohmic power dissipation.

Theory

The impedance of a CDI cell, as measured via EIS, can be described by the following equations, modified from Suss *et al.*[14]

$$Z_{2w} = Z_{EEI} + Z_{4w} \tag{1}$$

$$Z_{EEI} = R_{EER,s} + \frac{R_{contact}}{1 + i\omega R_{contact} C_{contact}} \tag{2}$$

$$Z_{4w} = R_{IER} + R_{sp} + 2\sqrt{R_{mA} Z_w} \coth\left(\sqrt{\frac{R_{mA}}{Z_w}}\right) \tag{3}$$

$$Z_w = \left(i\omega C_w + \frac{1}{R_{ct} + Z_{st}}\right)^{-1} \tag{4}$$

$$Z_{st} = \frac{R_{st}}{(i\omega\tau_{st})^n} \coth\left[(i\omega\tau_{st})^n\right] \tag{5}$$

where Z_{2w} and Z_{4w} are the total device impedance measured in two-wire and four-wire measurement modes, respectively, Z_{EEI} is the external electronic impedance, $R_{EER,S}$ is the series resistance of the external electronic impedance, $R_{contact}$ is the resistance of the contact between the current collectors and electrodes, $C_{contact}$ is the capacitance of the contact, ω is the angular frequency of the applied voltage sine wave, R_{IER} is the internal electronic resistance (e.g. in-plane resistance of the solid electrode), R_{sp} is the ionic resistance of the separator, R_{mA} is the electrode macropore ionic resistance, Z_w is the macropore wall impedance, C_w is the wall capacitance, R_{ct} is the resistance in parallel with ionic capacitance along the micropore wall (here called internal ionic-transfer resistance), Z_{st} is the storage pore impedance, R_{st} is the storage pore resistance, τ_{st} is the storage pore characteristic time,

and n is the anomalous diffusion order parameter.[54,55] The anomalous form of Z_{st} was needed to fit the low frequency impedance data, and accounts for the full effect of a distribution of storage resistances within the micropores of the material, though the fitted order parameter ranged from n = 0.38-0.48 (see supporting information Table S1), which is close to its non-anomalous value of n = 0.5. The CDI cell equivalent circuits corresponding to Eqns. (1-5) are illustrated in Fig. 1.

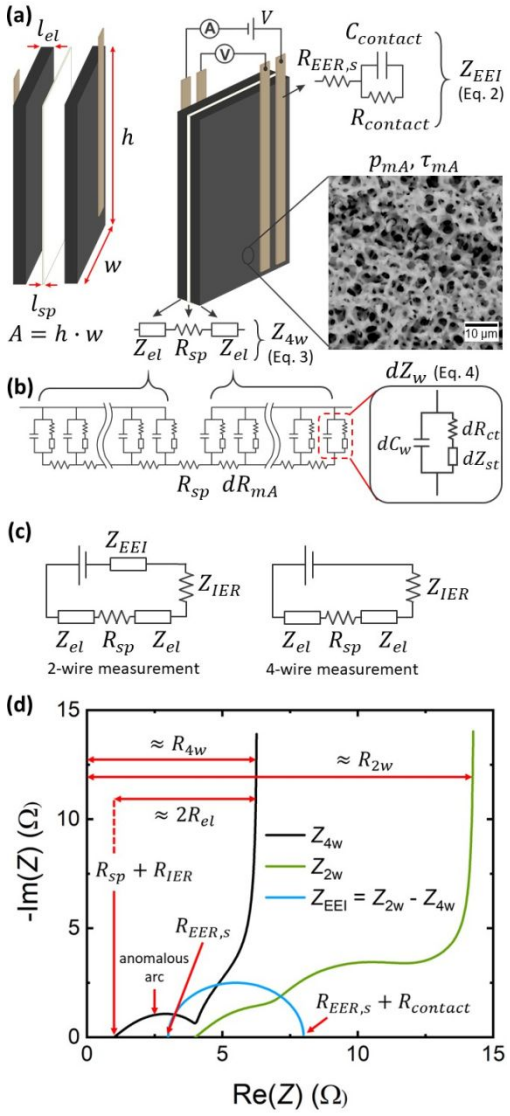

Figure 1: (a) An individual CDI cell with marked dimensional variables as well as a full cell in a four-wire measurement setup with impedances indicated from Eq. 2 and a SEM image of the electrode material. The activated HCAM material has macropore porosity p_{mA} and

tortuosity τ_{mA}. (b) The nested transmission line circuit model described by Eqns. 3-5. (c) The equivalent circuits for two-wire and four-wire measurment modes of a cell (Eqns. 1 and 3). d) Representative EIS spectra calculated from Eqns. 1-5 with $R_{sp} + R_{EER} = 1\ \Omega$, $R_{st} = 0.15\ \Omega$, $C_{st} = 4.5$ F, $R_{mA} = 7\ \Omega$, $R_{ct} = 0.3\ \Omega$, $C_w = 0.2$ F, $n = 0.5$, $R_{EER,s} = 3\ \Omega$, $R_{contact} = 5\ \Omega$, and $C_{contact} = 0.15$ F. These values were chosen to represent fits of measured spectra (Table S1). Resistance designations follow from Eqns. (6 - 8).

A simple interpretation of the cell impedance can be obtained by examining the real-component location of certain features in the Nyquist plot as illustrated in Fig. 1 (d). From this interpretation, the following resistances can be identified[56]

$$R_{4w} = R_{IER} + R_{sp} + 2R_{el} \quad (6)$$

$$R_{sp} = \frac{l_{sp}\tau_{sp}}{A\kappa p_{sp}} \quad (7)$$

$$R_{el} = \frac{l_{el}\tau_{mA}}{3Ap_{mA}}\frac{\kappa+\sigma}{\kappa\sigma} \approx \frac{l_{el}\tau_{mA}}{3Ap_{mA}}\frac{1}{\kappa} \quad (8)$$

where R_{el} is the resistance of one electrode, l_{el} is the thickness of an electrode, l_{sp} is the thickness of the separator, τ_{mA} is the tortuosity of the macropore structure,[48,57,58] A is the electrode face area, p_{sp} is the separator porosity, p_{mA} is the electrode macroporosity, κ is the electrolyte conductivity, and σ is the electrode conductivity (here 22 ± 8 S/cm). For our system, $\sigma \gg \kappa$ ($\sigma/\kappa \approx 10^4$), which means that $(\kappa + \sigma)/\kappa\sigma \approx 1/\kappa$. It is noteworthy that our electrodes have high electrical conductivity due to their monolithic structure. The approximation that the solid electrode resistivity is negligible compared to the ionic resistivity may not hold in other systems where the electrode resistivity can be several orders of magnitude higher ($\sigma/\kappa \approx 10^1$).[51] The factor of 2 in front of R_{el} in Eqn. 6 comes from the fact that there are two electrodes and the factor of 1/3 in Eqn. 8 comes from the

transmission-line physics associated with porous system charging.[56] We also note that the macroporosity (p_{mA}) and tortuosity (τ_{mA}) are often linked via an effective medium-type approximation.[59] For example, the Bruggeman approximation is often used,[56] which predicts that $\tau_{mA} = p_{mA}^{-1/2}$. Fig. 1 (a) schematically shows the cell construction and manifestations of various parameters in Eqns. (1-8) while Fig. 1 (d) shows the corresponding locations of Eqns. (6-8) on a Nyquist plot.

Experimental

Materials

We performed EIS measurements using hierarchical carbon aerogel monolith (HCAM) electrodes as a model system.[60–63] SEM images of the HCAM material used are shown in Fig. 1 (a) and Fig. S1. The bulk material characteristics underlying the material for the various electrode thicknesses investigated here are given in Table 1, where p_{tot} is the estimated total porosity of the electrode material, p_{mi} is the porosity of micropores, and p_{mA} is macropore porosity as defined in Eq. 8. For representative porosity characteristics, we refer to the prior work of Hawks *et al.*[63] For reporting specific capacitance in Table 1, we used 2M NaCl as the electrolyte for its ease of analysis and to have a more representative value when compared to previous measurements on the same materials system.[14]

Table 1: Electrode Material Properties*

l_{el} (μm)	A (cm^2)	Mass/electrode (g)	ρ (g/cm^3)	p_{tot}	p_{mi}	p_{mA}	C in 2 M NaCl (F/g)
355	5	0.103	0.580	0.702	0.17	0.532	84.1
600	5	0.164	0.547	0.720	0.17	0.550	87.7
1025	5	0.285	0.556	0.715	0.17	0.545	86.3

*p_{tot} is the total porosity calculated assuming ρ_{carbon} = 1.95 g/cm^3 and $p_{tot} = 1 - \rho/\rho_{carbon}$. Here p_{mi} is assumed to be 0.17 and p_{mA} is calculated from $p_{mA} = p_{tot} - p_{mi}$.[63]

Contact Resistance Characterization

We fabricated flow-through electrode CDI cells (fte-CDI) to test the impedance models and the effect of current collector contacts. Each cell was built using two 2 × 2.8 cm slices of HCAM with thicknesses between 350 and 500 μm. We separated the HCAM electrodes with 90 μm polyester plastic mesh (McMaster-Carr 9218T73). Each electrode was placed in contact with two current collectors made of either titanium foil,[61] gold wire, or graphite foil (Panasonic EYG-S121803DP). The assembly of electrodes, separator, and current collectors, seen in Fig. 1 (a), was sandwiched between two acrylic plates and the cell was sealed with epoxy.[61,63] Inlet and outlet ports were cut into the acrylic plates to allow for water flow through the cell.

In preparation for impedance measurements, we conditioned the cells by performing at least 10 cyclic voltammetry (CV) cycles at 1 mV/s between ± 0.8 V with 1.9 mL/min flow of 20 mM NaCl. We then discharged the cells at 0 V for at least 30 min and sealed them with 20 mM NaCl inside. Cell impedance was characterized by EIS using a BioLogic VSP-300 potentiostat, applying a 10 mV amplitude sinusoidal voltage at 0 V bias over the frequency range from 700 kHz to 40 mHz. Four-wire measurements were performed by connecting the sense and source probes to two separate current collectors as shown in Fig. 1 (a) while in two-wire measurements the sense and source probes were shorted together externally.

Separator and Electrode Resistance Characterization

For electrode and separator characterization, two 2 × 2.5 cm HCAM slices of thickness 355, 600, or 1025 μm (Table 1) were separated by polyester plastic mesh and contacted with a four-point probe. We placed the electrode-separator assembly in a sealed and stirred beaker containing 0.5-1 L of NaCl solution with concentration varying from 15 mM to 2000 mM. Some tests were also performed in 15mM solutions of NaBr and NaF. Importantly,

before we measured impedance, the electrodes were conditioned by performing 3-6 CV cycles at 1 mV/s between ± 0.8 V and discharged at short circuit for 30-45 min. Impedance was measured using a 10 mV sinusoidal voltage signal at 0 V bias, scanning over the frequency range from 700 kHz to 40 mHz.

Results and Discussion

Contact Resistance

The impedance spectra of CDI cells in aqueous NaCl electrolytes have several distinct features as seen in Fig. 2. The main features are one or two medium to high-frequency arcs, a real-component offset which comes from a combination of electronic and separator resistances, a $\sim$22-45° linear section due to electrode ionic resistance (sometimes not visible due to contact or internal ionic-transfer arcs),[14] and a nearly vertical line at low frequency due to the capacitive nature of the device. Confounding previous studies is the fact that the two high-frequency arcs are not always observed and are often confused with one another. The presence of the high-frequency arc(s) depends on electrode material, current collector material, and testing conditions. As we will discuss below, our measurements suggest that one of these arcs is due to the resistance and parallel capacitance nature of the contact between the current collector and electrode. The second is likely an ionic transfer mechanism within the electrode itself which we will discuss below.

We use the four point probe to deconvolute the external electronic impedance (Z_{EEI}) from the resistances inside the cell. To this end, we subtract the four-wire impedance (Z_{4w}) from the two-wire impedance (Z_{2w}). This operation allows us to isolate Z_{EEI} and definitively identify which features of the impedance spectra are due to current collector contact effects and which are due to internal cell processes. Fig. 2 shows representative Z_{EEI} curves for CDI

cells built with different current collector materials: titanium foil, gold wire, and graphite paper (graphoil). Several cells were built with each material and all showed Z_{EEI} curves similar to those in Fig. 2. It is clear from Figs. 2 (a) and 2 (b) that contacts with gold wire and graphoil have a negligible capacitive component and act as pure resistors with Im(Z_{EEI}) ≈ 0 at all frequencies measured. However, the contact between titanium foil and the HCAM has a significant parallel *RC* component as shown by the arc in Fig. 2 (c). Furthermore, the impedance arc due to $R_{contact}$ with Ti contacts grows with time, resulting in an increased R_{EER} and therefore a higher total cell power loss (Fig. 3). The growth in external electronic resistance with a Ti current collector occurred without applied voltage or flow of electrolyte and did not manifest in cells with Au wire or graphoil current collectors (Fig. 4 (a)). As observed in Fig. 3, all of the change in Z_{EEI} over time with Ti contacts occurred in the contact arc, while the real intercept at high-frequency remained constant, indicating that it was the physical contact between the Ti and HCAM electrode that degraded over time, rather than $R_{EER,S}$.

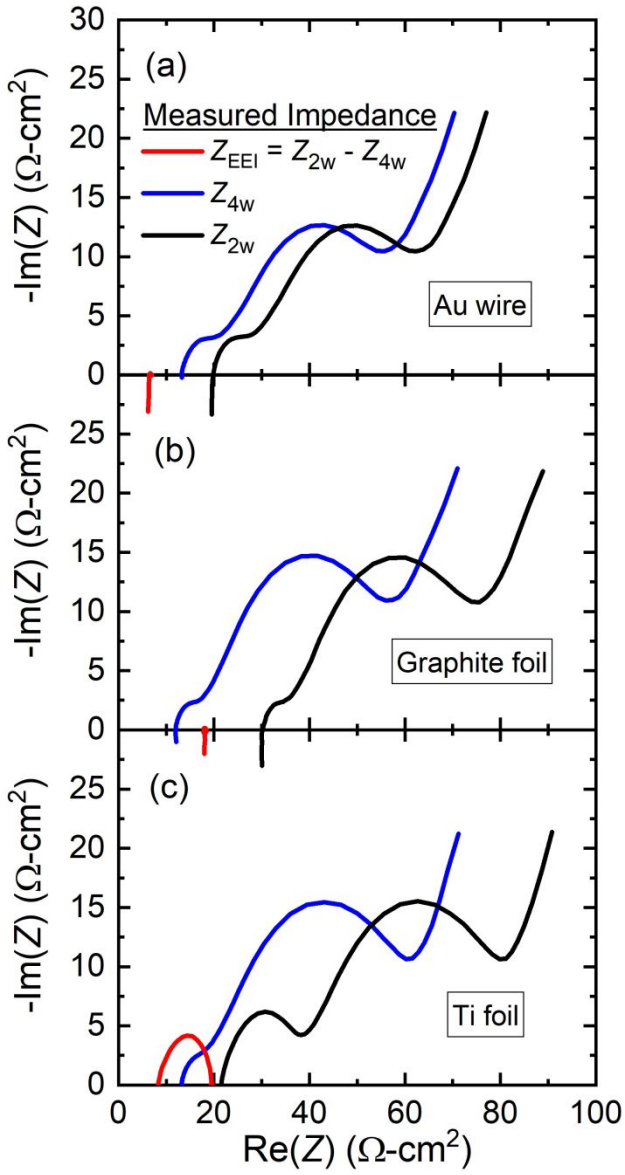

Figure 2: Representative EIS spectra of CDI cells with different current collector materials. All cells measured demonstrated similar bahavior. Each cell contained two 2 × 2.8 cm electrodes and was tested in stagnant 20mM NaCl.

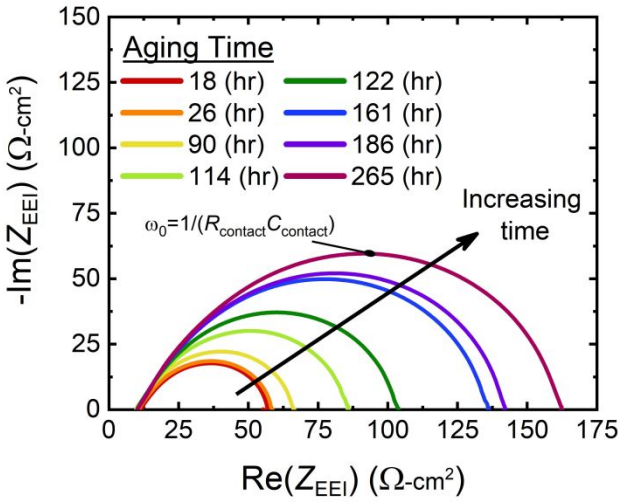

Figure 3: The change over time of the external electronic impedance (dominated by contact impedance) of a CDI cell with Ti foil current collectors (i.e. time evolution of the red arc in Fig. 4 (c)). The time corresponds to that elapsed since the initial conditioning of the electrodes. Between measurements, the cell was left stagnant in 20mM NaCl solution.

Extracted values of $R_{contact}$ and $C_{contact}$ over time can be found in Figs. 4 (a) and 4 (b).

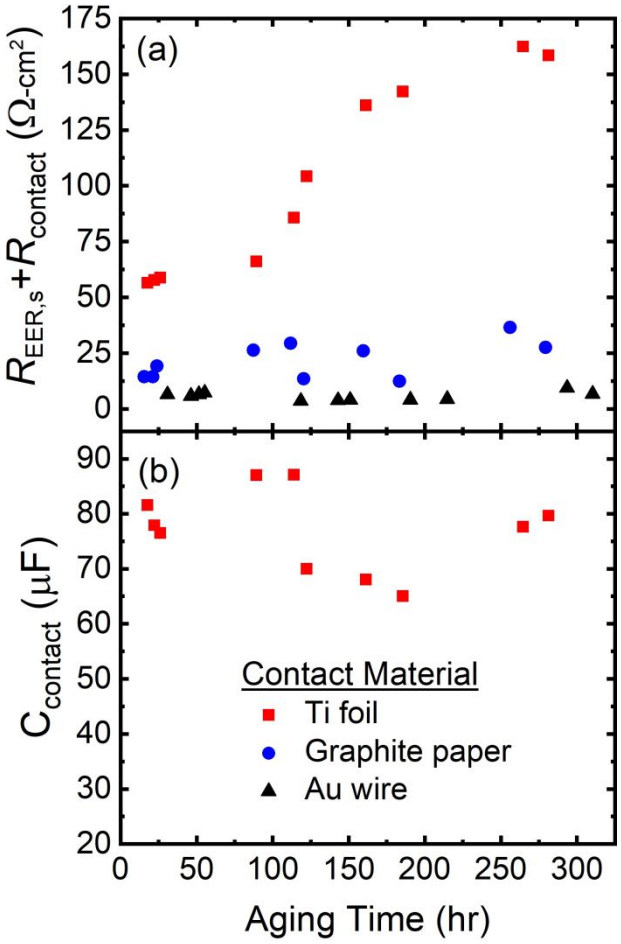

Figure 4: (a) Contact degradation over time for CDI cells with three different current collector materials. The time is that elapsed since the initial conditioning of the electrodes. Between measurements, the cell was left stagnant in 20 mM NaCl solution. (b) The change over time of the contact capacitance ($C_{contact}$) of the CDI cell with Ti foil current collectors in (a). The data was extracted from the impedance curves shown in Fig. 3 by using the resonance frequency at the top of the arc and the measured resistance ($\omega_0 = 1/R_{contact}C_{contact}$).

The *RC* arc observed with the Ti contact could indicate that there is a gap between the current collector and the HCAM electrode. Interestingly, though, an investigation of contact resistance in different electrolyte concentrations (Fig. 5) shows that the controlling element between the Ti foil and the HCAM contact does not depend on solution conductivity, which suggests a solid-state origin (e.g. oxidation) as the source of the impedance arc. This finding is also supported by the fact that the feature only occurs with

the Ti current collectors, which are known to oxidize more than gold or graphite. Furthermore, if the capacitive behavior were related to cell design or caused by a physical peeling apart of the electrode and current collector, the effect would likely be contact-material independent. However, since the degradation is seen only with Ti current collectors, it suggests a contact-material specific cause. Interestingly, the capacitance of the Ti current collector contact does not change significantly with time (Fig. 4 (b)), remaining at ~80 μF after 300 hours of aging. The stable capacitance over time is certainly inconsistent with uniform oxide growth, which would likely lead to a decrease in capacitance as the passivation layer grew thicker. One possible mechanism is that a localized passivating oxide layer increases in resistivity over time but does not appreciably change dimensions. Regardless of the mechanism causing it, the presence and growth over time of a contact impedance arc indicates that Ti is not a good current collector material for CDI.[64–66]

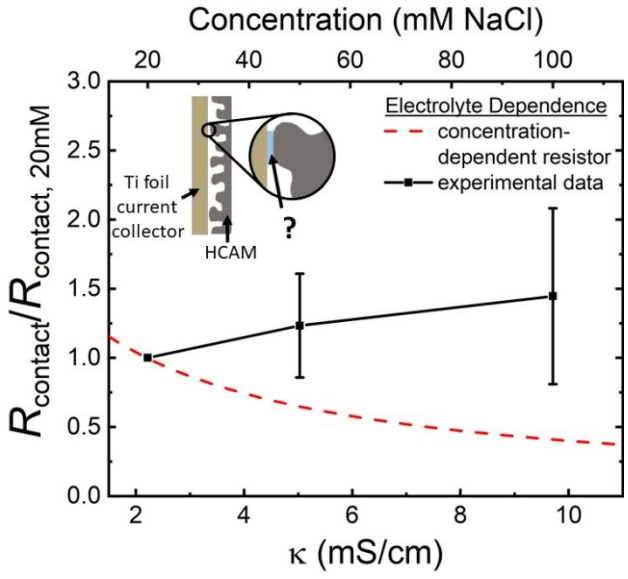

Figure 5: Relative contact resistance of CDI cells with Ti foil current collectors in different concentration NaCl electrolytes (solid line). The dashed line shows the theoretical dependence of contact resistance on solution conductivity if the spacer was electrolyte based. The dependence of $R_{contact}$ on electrolyte conductivity suggests that the substance

separating the HCAM electrode from the Ti current collector is not electrolyte. Error bars are one standard deviation

Internal Ionic-Transfer Resistance

By using four-wire measurements, we can factor out anomalous contact effects like that shown for the Ti electrodes above or that observed by Qu *et al.*[48] and Gaberscek *et al.*[49] Thus, we now examine the remaining arc, which we attribute to an internal ionic-transfer resistance. To separate ionic-transfer from other resistances in the cell, we fit the model described by Eqns. (3-5) to impedance measurements performed in a four-wire measurement mode. Fig. 6 (a) presents such fits to Eqns. (3-5) of impedance data taken from a two-electrode assembly (l_{el} = 1025 μm) in 50-2000 mM NaCl solutions. We chose to examine fit parameters over a wide range of electrolyte solution resistivities because an obvious linear relationship similar in form to Eqns (7,8) is expected between at least some of the fit parameters (e.g., R_{mA}, R_{sp}) and electrolyte conductivity. While the numerous fitting parameters of Eqns. (3-5) make reliable parameter extraction difficult, Fig. 6 (b) generally demonstrates the expected linear scaling with electrolyte resistivity. It is the scaling of these various resistors, and in particular R_{mA}, that cause the impedance spectrum to shift so dramatically in Fig. 6 (a). From this analysis, we find that the storage pore resistance R_{st} is insignificant compared to series resistance (R_{sp} + R_{IER}) and R_{mA} (Fig. 6 (b)), which was also found by Suss *et al.*[14] with activated HCAM materials like the ones examined here. For further confidence in the fitting procedure, we also plot in Fig. 6 (b) linear fits (solid lines) in order to highlight the observed expected relationship between parameters like R_{mA} and R_{sp} and solution resistivity. It is noteworthy that the fitting parameter C_w is on the order of 0.1 F, which is too small to be a micropore effect and too large to be a stray capacitance. Such a value is plausible as the capacitance of the macropore walls, which is consistent with the original assignment of Suss *et al.*[14] for a weakly activated material.[63]

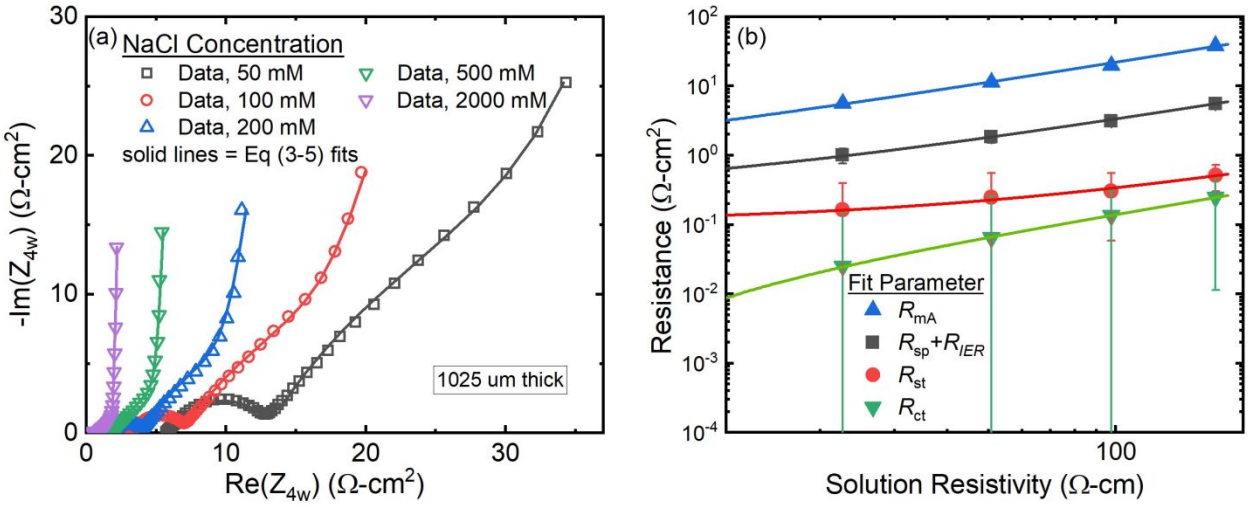

Figure 6: (a) EIS spectra from a 2×2.5 cm two electrode cell (l_{el} = 1025 μm) contacted with a 4-point probe in a stirred 0.5-1 L beaker containing 50-2000 mM NaCl concentrations in deionized water. (b) Resulting resistance values from full fits to Eqns. (3-5). Error bars come from the uncertainty of the fits. The full list of parameters used to fit the EIS spectra can be found in Table S1. The lines in (b) are linear fits to the fitted resistance value vs. solution resistivity.

Interestingly, we find that this internal ionic-transfer resistance R_{ct} is the lowest resistance of the system and yet is responsible for the small arc at medium-high frequency in Fig. 6 (a), caused by its parallel combination with the electrode wall capacitance C_w. Our model shows that R_{ct} has a significant impact on the shape of the EIS curve with a small change in the internal ionic-transfer resistance (Fig. S2). The difference between the direct interpretation of the ionic-transfer arc, in which R_{ct} is equal to the width of the arc, and the true value of R_{ct} as found by the modified Suss et al.[14] model is due to the fact that R_{ct} is embedded in the nested transmission line model of the porous electrode, as seen in Fig. 1(b). Many models place R_{ct} in series with the transmission line, similar to where we place $R_{contact}$; however this would imply a different mechanism behind R_{ct}, essentially mislabeling the contact resistance as an ionic-transfer process. This difference in interpretation of R_{ct} is crucial because the more straightforward interpretation would lead one to believe that it is a significant contributor to overall Ohmic power dissipation (Fig. S2). The model of R_{ct} used

herein implies that the internal ionic-transfer resistance represents a hindrance to the ions entering the storage pores (micropores) of the electrode whereas other models would indicate that R_{ct} is not necessarily originating from entry into the micropores.[18]

The hypothesis of a hindrance to storage pore entrance has a plausible molecular mechanism. For example, at sufficiently high applied potentials, solvation shell layers of ions need to be distorted for these to fit into small pores, as suggested by Suss *et al.*[14] A second plausible (and not necessarily independent) possible mechanism is a transit time delay of ions moving from macropores to micropores, which would help explain the observed dependence of R_{ct} on electrolyte resistivity in Fig. 6b[19] To explore the former mechanism further, we performed experiments with several ions of varying solvation energies. As shown in Figure 7, we found that internal ionic-transfer resistance decreases with decreasing strength of hydration. Further, we found that the ionic-transfer arc is significantly less pronounced with more strongly activated of the electrodes (Fig. S3), which are known have a wider micropore size distribution.[14] We caution that this effect may not be the same in other systems, particularly non-CDI electrodes in which diffusion through surface films on the electrodes may be the cause of the mid to high-frequency arc.[67] Our observations also suggest that a voltage-dependent study (and comparison of EIS spectra for ions of varying solvation) could shed light on the origin of R_{ct} as an applied electric field would be expected to lower the activation energy of the process, which has been observed previously by Suss *et al.*[14,68] In any case, our conclusion is that R_{ct} has a small contribution to Ohmic power dissipation.

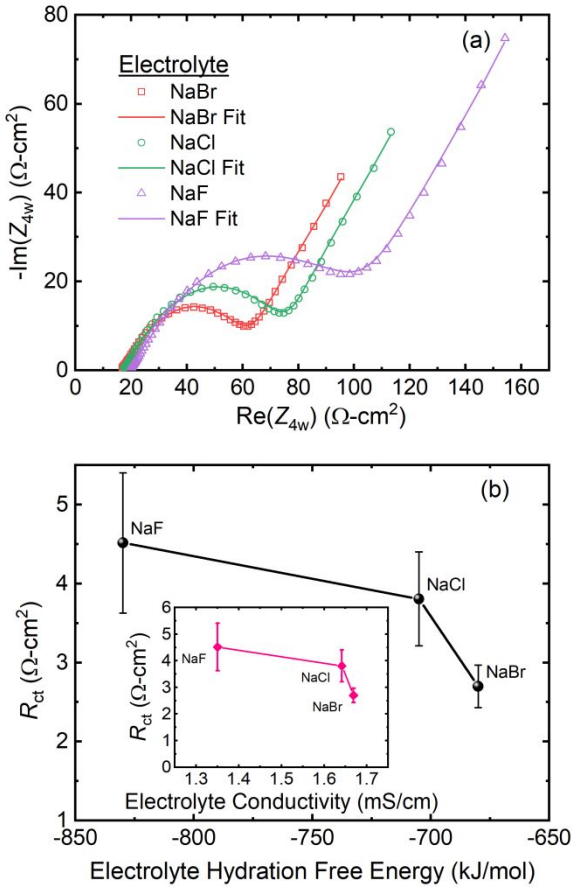

Figure 7: (a) EIS spectra from 2×2.5 cm two electrode cell (l_{el} = 1025 μm) in a stirred beaker of 15 mM electrolyte with fits from Eqns (3-5). The full set of fitting parameters are shown in Table S1. (b) Internal ionic-transfer resistance, extracted from the fits in (a), plotted against total hydration free energy of the electrolyte and electrolyte conductivity (inset).[69]

Since we can now be confident that R_{ct} is a negligible contributor to Ohmic dissipation, we turn to an analysis of the primary resistances in the CDI cell. For this we use a simpler interpretation of EIS curves, described by Fig. 1 (d) and Eqns. (6-8), which does not involve complex fitting procedures.

Series Resistance

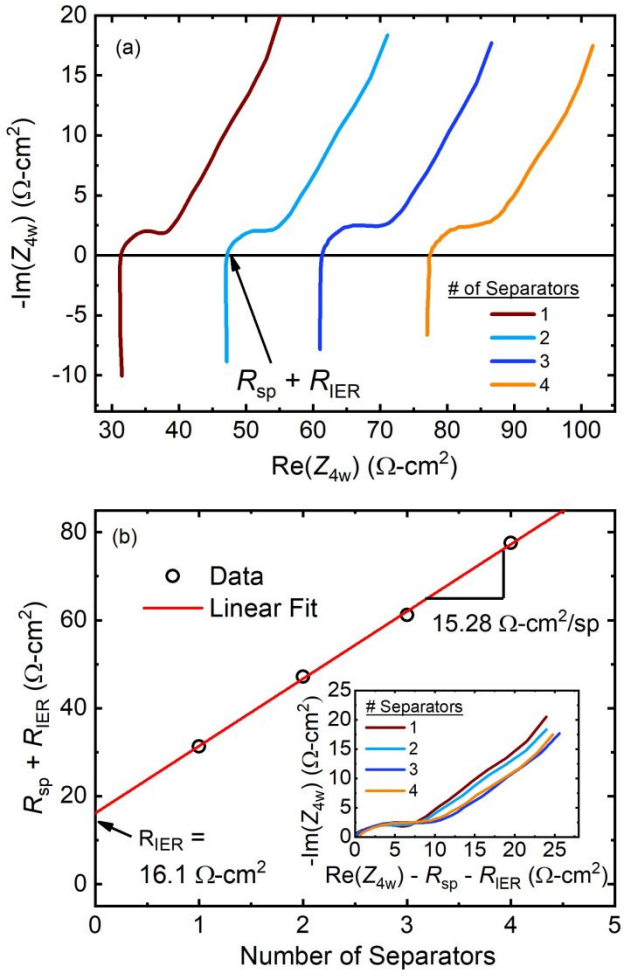

Figure 8: (a) EIS spectra of two 2 × 2 cm electrodes with different numbers of separators stacked between them. (b) The value of the internal series resistance (R_{sp} + R_{IER}) plotted against number of separators. The slope of the line gives the resistance per separator used. The inset shows the spectra from (a) with R_{sp} +R_{IER} subtracted. This data is also presented by Hawks *et al.*[62] in their supplementary information.

From the full EIS fits performed to extract charge-transfer resistance, we have established that the simple analysis of Fig. 1 (d) is applicable. We can now use this analysis to extract series resistance, here defined as the sum of external electronic resistance (R_{EER}), internal electronic resistance (R_{IER}), and separator resistance (R_{sp}). In particular, we focus on the internal series resistance (R_{IER} + R_{sp}), which excludes the external electronic resistance and the complex nature of the contact resistance. From Fig. 6, the internal series resistance (R_{IER}

+ R_{sp}) was the second largest contributor to total cell resistance as measured in fourwire mode. By examining the measured real and imaginary parts of the four-wire impedance at high-frequency, we obtain the internal series resistance $R_{IER}+R_{sp}$ from the intersection of the curve with Im(Z_{4w}) = 0. By plotting the intercept for multiple separator thicknesses, we are able to decouple the separator and internal electronic resistances.[62] Fig. 8 (a) shows EIS spectra taken on a 2×2 cm HCAM assembly in 20 mM (2.4 mS/cm) NaCl solution with 1025 μm thick electrodes. From Fig. 8 (a), it is clear that increasing the number of separators shifts the impedance curve to higher resistances without substantially changing the shape of the Nyquist plot. This is further emphasized by the inset of Fig. 8 (b), which shows that the impedance curves overlay one another to a reasonable degree when the internal series resistance ($R_{IER}+R_{sp}$) is subtracted out. As expected, the internal series resistance is linearly dependent on separator thickness, where here the slope reveals the resistance of an individual separator (R_{sp}) and the intercept reveals the internal electronic resistance, R_{IER} (Fig. 8 (b)). Here we attribute the internal electronic resistance (R_{IER}) to in-plane current flow in the HCAM electrode due to the finite distance between the distributed area of the electrode and the points of contact of the four-wire setup (Fig. 1).

Ionic Resistance within the Electrodes and Tortuosity

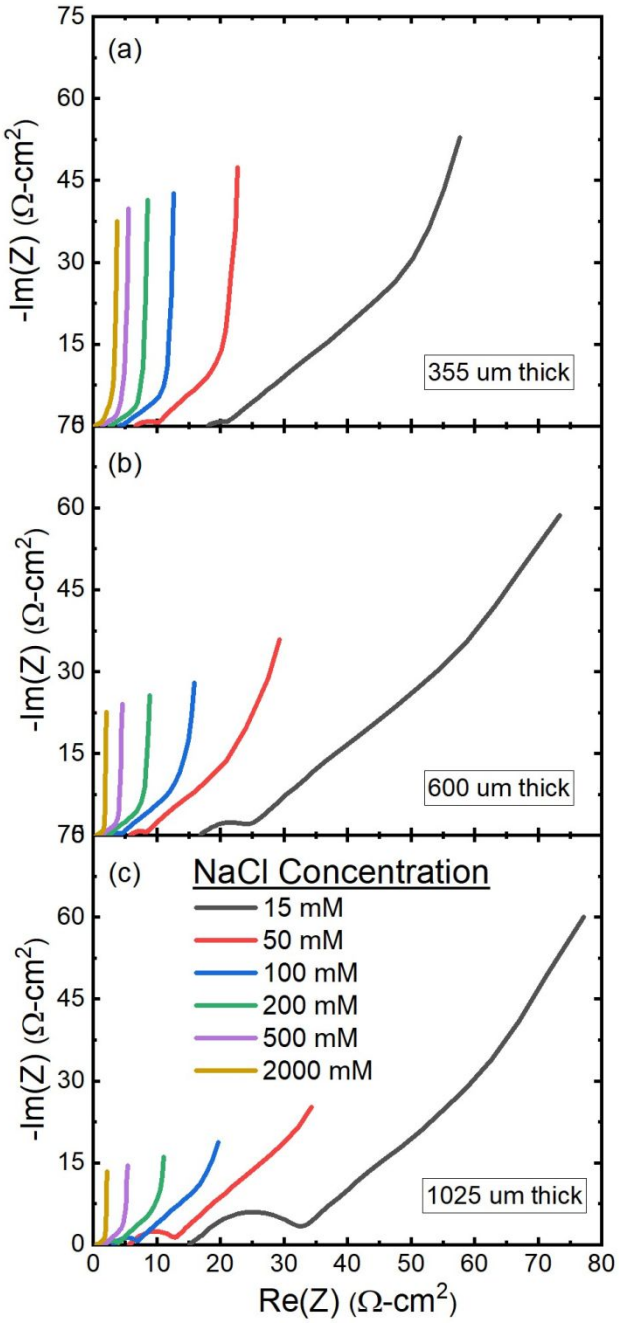

Figure 9: EIS spectra from 2×2.5 cm two electrode cells (l_{el} = 355, 600, 1025 μm) contacted with a 4-point probe in a stirred beaker containing 0.5-1 L of 50-2000 mM NaCl. The data in (c) is identical to that in Fig. 6 (a).

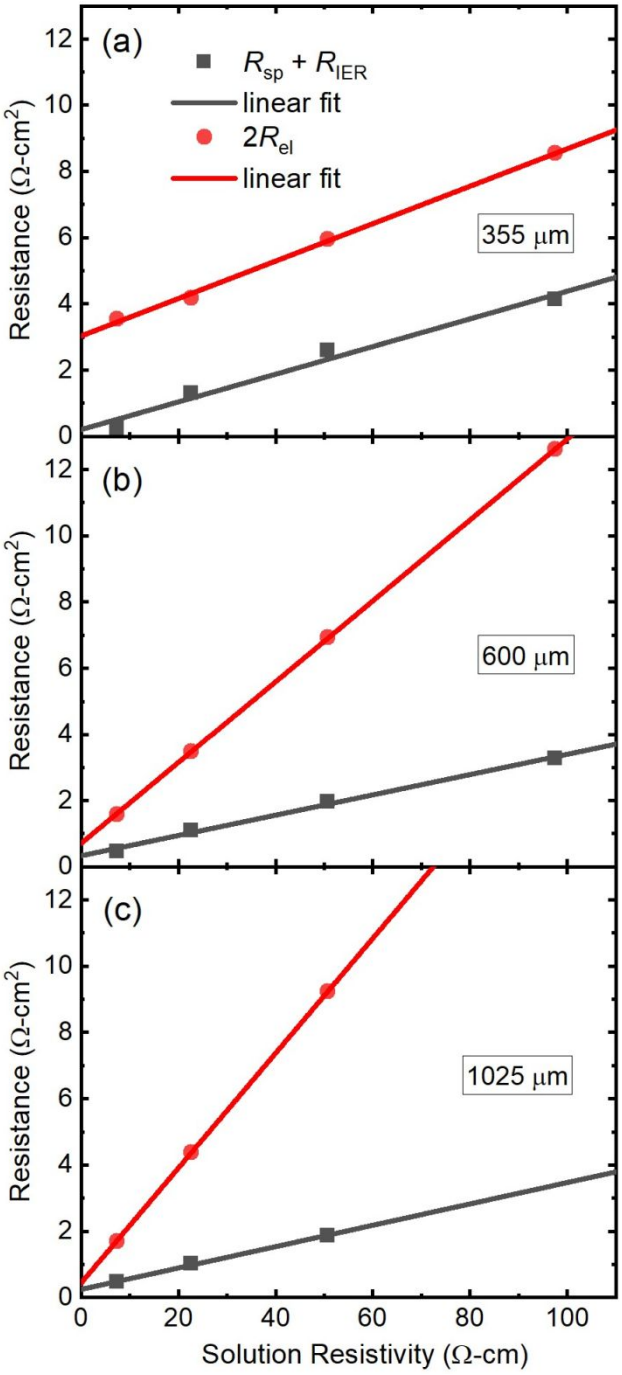

Figure 10: Results from extracting R_{el} and internal series resistance (R_{IER} +R_{sp}) from Fig. 9 according to the definitions in Fig. 1(d) and Eqns. 7 and 8 for different thickness electrodes.

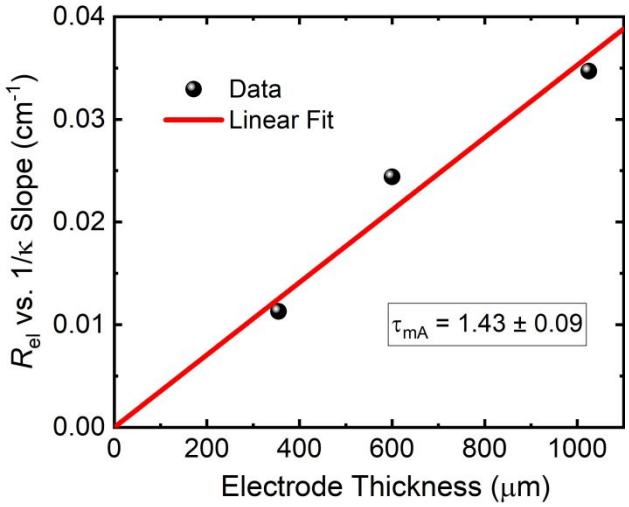

Figure 11: The overall electrode material tortuosity obtained by examining the slope of R_{el} vs. $1/\kappa$ from Fig. 10 as a function of electrode thickness. The linear fit was forced to have a zero intercept. The slope corresponds to an average electrode material tortuosity of 1.43 ± 0.09, which is consistent with an effective Bruggeman porosity of p_{mA} = 0.54 which is very close to the value we estimate through material density and microporosity (Table 1).[56]

We now turn our simplified analysis toward the electrode macropore ionic resistance, which is the largest contributor to the total Ohmic dissipation in our devices when measured in a four-wire configuration (Fig. 6). We explored the electrode material properties responsible for this resistance by testing different electrode thicknesses and electrolyte concentrations. Fig. 9 plots all the EIS data taken for three different electrode thicknesses (l_{el} = 355, 600, 1025 μm) over a wide NaCl concentration range (15-2000 mM). Notably, only the thicker electrodes displayed a pronounced R_{ct} arc at mid to high frequencies. While this appears to be a prominent feature, in fact it is small compared to the other resistances in the system (Fig. 6). Because here R_{ct} and R_{st} are small compared to the electrolyte resistance in the pores, we can estimate R_{el} according to Eqns. (6-8) and Fig. 1 (d). Fig. 10 displays the results of extracting $2R_{el}$ and $R_{IER} + R_{sp}$ from Fig. 9 according to the definition in Fig. 1(d) and Eqn. 6. Note that only the curves which turned up sufficiently

steeply could be analyzed, and thus all the 15 and 50 mM data and the 100 mM curve for the 1025 μm thick electrode were exempt from analysis.

Fig. 10 clearly shows that $2R_{el}$ as obtained by the simple analysis from Fig. 9 is linear with solution resistivity (measured by a bench-top electrolyte conductivity probe), as expected from Eqn. 8. Thicker electrodes, while expected to provide a larger capacitance, also have a much larger increase of $2R_{el}$ with increasing solution resistivity, creating a trade-off in cell design. Using the slopes obtained from Fig. 10 and assuming constant tortuosity, we extract the average tortuosity of the electrode macropores by plotting the slope of $2R_{el}$ vs. $1/\kappa$ against electrode thickness, where the slope is equal to $2l_{el}\tau_{mA}/3Ap_{mA}$. This analysis gives a slope of the best-fit line equal to $2\tau_{mA}/3Ap_{mA}$, which reveals a material tortuosity of 1.43 ± 0.09 (Fig. 11), using the average p_{mA} value for the material from Table 1. This value is in excellent agreement with the Bruggeman approximation of 1.36 using a constant macroporosity of 54%. The value of tortuosity found here (1.43 ± 0.09) is significantly lower than that previously estimated for carbon aerogels (~3.5),[48,70] but is consistent with the SEM images (Fig. S1) showing an open and highly porous network. Overall, this suggests that our HCAM materials are excellent for minimizing electrode ionic resistances, which as discussed above are a major contributor to overall cell resistance.

Overall Resistance Breakdown and Implications for Cell Design

Finally, with an understanding of what each feature of the EIS spectrum represents, we now analyze their relative impacts for our CDI cell design. The resistance breakdown presented in Eqns. (6-8) has important implications for prioritizing which resistances to minimize, especially when considering how to scale devices from the laboratory bench to practical commercial sizes. We note that this analysis applies to low-frequency electrical operation where significant depletion of the electrolyte does not occur. Fortunately, such a situation

is applicable to a wide range of CDI operation.[71–73] Given these assumptions, we find that electrode ionic resistance is the largest contributor to the overall resistance picture; though, for this to be the case, it is essential that the external electronic and contact resistances be minimized (Fig. 12).

In order to obtain a sense of how the overall resistance picture changes with the electronic component, Fig. 12 plots the relative power consumption of the respective elements versus the electronic resistance of the device. Since electronic resistance is highly dependent on device design and assembly, we examine its impact by varying its value over three orders of magnitude. In terms of scaling, the relative power consumption plotted in Fig. 12 is understood from

$$P = J^2R \tag{9}$$

where P is the power density (mW/m^2), J is the current density (mA/cm^2), and R is the relevant resistance of Fig. 1 multiplied by the electrode face-area (Ω-cm^2). Notably, Eq. (9) ignores how R depends on the applied frequency of J.[74,75] Nevertheless, from Eq. 9 it is clear that power dissipation density is related to area-normalized resistance in Ω-cm^2. We note that while electrode and separator resistances scale inversely with the electrode face area, in practice the external electronic resistances are unlikely to decrease as rapidly with increasing electrode size, making their relative contribution to overall power dissipation likely higher with larger electrode size. Fortunately, though, external electronic resistances can be engineered to be quite low.[8]

Lastly, our conclusion that R_{el} is larger than the separator resistance is opposite to the results of Dykstra *et al.*,[51] who found that the resistance in the separator was largest in a MCDI cell. There are several possible reasons for this discrepancy. Dykstra *et al.*[51] modeled and tested MCDI cells in which, during operation, the ion concentration is higher in the electrode macropores than in the separator channel, which is likely not the case for

membrane-free cells. Furthermore, the separators used by Dykstra are more than three times the thickness of our separators due to the differences in cell architecture. Perhaps most importantly, Dykstra's model initially did not consider how the current varies across a porous electrode.[51] Later, when these factors are accounted for, the ionic resistance in the electrodes was found to be significantly higher and more comparable to the separator resistance.[52]

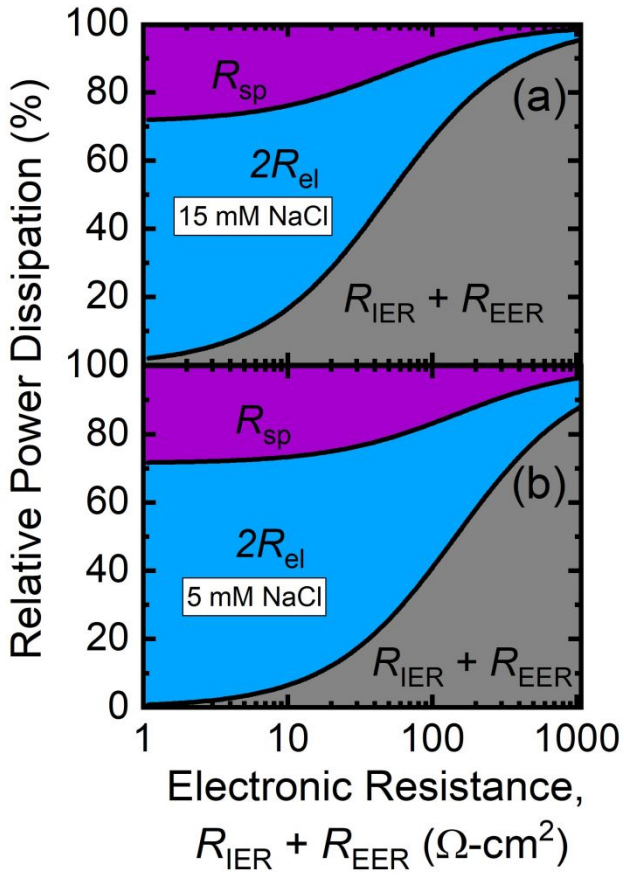

Figure 12: A breakdown of the total cell resistance for different electronic resistances (R_{IER} + R_{EER}). Separator and electrode resistances were calculated using Eqns. 7 and 8 with l_{sp} = 90 μm, l_{el} = 350 μm, τ_{sp} = 1.2, τ_{mA} = 1.36, p_{sp} = 0.47, p_{mA} = 0.55, and κ = 1.684 mS/cm.
The relative power dissipation is defined using Eq. 9 and considering the total cell resistance as defined in Eqn. (6) and Fig. 1.

Conclusion

We have presented a theoretical and experimental breakdown of the resistances within a CDI cell. We found that the anomalous high-frequency arc often seen in the impedance spectra of a CDI device can be either due to the contact impedance between the current collector and electrodes or due to an internal ionic-transfer resistance. In our system, we assign the ionic-transfer resistance to a hindrance impeding the ions from entering the storage micropores of the activated carbon electrode. We separate these effects by comparing two-wire and four-wire measurements and find that titanium current collectors are not ideal because the contact resistance grows significantly over time. We further investigate the nature of internal ionic-transfer resistance and find that it is negligible compared to other cell resistances. Additionally, we examined the other cell resistances that contribute to the total cell Ohmic power loss to understand their relative impact. In our system, we find that the ionic resistances within the electrode are the largest contributor to the total cell resistance for a reasonably low external electronic resistance (< 20 Ω-cm^2). Overall, this work outlines a comprehensive framework for extracting all the various contributors to the overall cell Ohmic power dissipation, which is a powerful tool for future CDI cell optimization and scale-up.

Acknowledgments

This work was performed under the auspices of the U.S. Department of Energy by Lawrence Livermore National Laboratory under Contract DE-AC52-07NA27344. Work at LLNL was supported by LLNL LDRD 18-ERD-024 and the California Energy Commission grant ECP16-014. Support was also provided by the Mickey Leland Energy Fellowship Program and the Materials and Chemistry Institute summer internship program.

References

(1) Bales, C.; Kovalsky, P.; Fletcher, J.; Waite, T. D. Low cost desalination of brackish groundwaters by Capacitive Deionization (CDI) - Implications for irrigated agriculture. *Desalination* **2019**, *453*, 37–53.

(2) Tan, C.; He, C.; Tang, W.; Kovalsky, P.; Fletcher, J.; Waite, T. D. Integration of photovoltaic energy supply with membrane capacitive deionization (MCDI) for salt removal from brackish waters. *Water Res.* **2018**, *147*, 276–286.

(3) Oyarzun, D. I.; Hemmatifar, A.; Palko, J. W.; Stadermann, M.; Santiago, J. G. Ion selectivity in capacitive deionization with functionalized electrode: Theory and experimental validation. *Water Research X* **2018**, *1*.

(4) Oyarzun, D. I.; Hemmatifar, A.; Palko, J. W.; Stadermann, M.; Santiago, J. G. Adsorption and capacitive regeneration of nitrate using inverted capacitive deionization with surfactant functionalized carbon electrodes. *Separation and Purification Technology* **2018**, *194*, 410–415.

(5) Palko, J. W.; Oyarzun, D. I.; Ha, B.; Stadermann, M.; Santiago, J. G. Nitrate removal from water using electrostatic regeneration of functionalized adsorbent. *Chemical Engineering Journal* **2018**, *334*, 1289–1296.

(6) Hand, S.; Cusick, R. D. Emerging investigator series: capacitive deionization for selective removal of nitrate and perchlorate: impacts of ion selectivity and operating constraints on treatment costs. *Environmental Science: Water Research & Technology* **2020**,

(7) Hand, S.; Guest, J. S.; Cusick, R. D. Technoeconomic Analysis of Brackish Water

Capacitive Deionization: Navigating Tradeoffs between Performance, Lifetime, and Material Costs. *Environ Sci Technol* **2019**, *53*, 13353–13363.

(8) Hemmatifar, A.; Ramachandran, A.; Liu, K.; Oyarzun, D. I.; Bazant, M. Z.; Santiago, J. G. Thermodynamics of Ion Separation by Electrosorption. *Environ. Sci. Technol.* **2018**, *52*, 10196–10204.

(9) Wang, L.; Dykstra, J. E.; Lin, S. Energy Efficiency of Capacitive Deionization. *Environ. Sci. Technol.* **2019**, *53*, 3366–3378.

(10) Hemmatifar, A.; Palko, J. W.; Stadermann, M.; Santiago, J. G. Energy breakdown in capacitive deionization. *Water Res.* **2016**, *104*, 303–311.

(11) Posey, F. A.; Morozumi, T. Theory of Potentiostatic and Galvanostatic Charging of the Double Layer in Porous Electrodes. *J. Electrochem. Soc.* **1966**, *113*, 176–184.

(12) Huang, Q.-A.; Li, Y.; Tsay, K.-C.; Sun, C.; Yang, C.; Zhang, L.; Zhang, J. Multiscale impedance model for supercapacitor porous electrodes: Theoretical prediction and experimental validation. *J. Power Sources* **2018**, *400*, 69–86.

(13) Kant, R.; Singh, M. B. Theory of the Electrochemical Impedance of Mesostructured Electrodes Embedded with Heterogeneous Micropores. *J. Phys. Chem. C* **2017**, *121*, 7164–7174.

(14) Suss, M. E.; Baumann, T. F.; Worsley, M. A.; Rose, K. A.; Jaramillo, T. F.; Stadermann, M.; Santiago, J. G. Impedance-based study of capacitive porous carbon electrodes with hierarchical and bimodal porosity. *J. Power Sources* **2013**, *241*, 266–273.

(15) Song, H.; Jung, Y.; Lee, K.; Dao, L. Electrochemical impedance spectroscopy of porous electrodes: the effect of pore size distribution. *Electrochim. Acta* **1999**, *44*, 3513–3519.

(16) Song, H.; Hwang, H.; Lee, K.; Dao, L. The effect of pore size distribution on the frequency dispersion of porous electrodes. *Electrochim. Acta* **2000**, *45*, 2241–2257.

(17) Yoon, S.; Jang, J.; Ka, B.; Oh, S. Complex capacitance analysis on rate capability of electric-double layer capacitor (EDLC) electrodes of different thickness. *Electrochim. Acta* **2005**, *50*, 2255–2262.

(18) Paasch, G.; Micka, K.; Gersdorf, P. Theory of the electrochemical impedance of macrohomogeneous porous-electrodes. *Electrochim. Acta* **1993**, *38*, 2653–2662.

(19) Mei, B.-A.; Munteshari, O.; Lau, J.; Dunn, B.; Pilon, L. Physical Interpretations of Nyquist Plots for EDLC Electrodes and Devices. *J. Phys. Chem. C* **2018**, *122*, 194–206.

(20) Cooper, S. J.; Bertei, A.; Finegan, D. P.; Brandon, N. P. Simulated impedance of diffusion in porous media. *Electrochim. Acta* **2017**, *251*, 681–689.

(21) Liu, Y.; Nie, C.; Liu, X.; Xu, X.; Sun, Z.; Pan, L. Review on carbon-based composite materials for capacitive deionization. *RSC Adv.* **2015**, *5*, 15205–15225.

(22) Porada, S.; Borchardt, L.; Oschatz, M.; Bryjak, M.; Atchison, J. S.; Keesman, K. J.; Kaskel, S.; Biesheuvel, P. M.; Presser, V. Direct prediction of the desalination performance of porous carbon electrodes for capacitive deionization. *Energy Environ. Sci.* **2013**, *6*, 3700.

(23) Wang, S.; Zhang, L.; Han, F.; Li, W.-C.; Xu, Y.-Y.; Qu, W.-H.; Lu, A.-H. Diaminohexane-Assisted Preparation of Coral-like, Poly(benzoxazine)-Based Porous Carbons for Electrochemical Energy Storage. *ACS Appl. Mater. Interfaces* **2014**, *6*, 11101–11109.

(24) Yoo, H. D.; Jang, J. H.; Ryu, J. H.; Park, Y.; Oh, S. M. Impedance analysis of porous carbon electrodes to predict rate capability of electric double-layer capacitors. *J. Power Sources* **2014**, *267*, 411–420.

(25) Liu, P.-I.; Chung, L.-C.; Ho, C.-H.; Shao, H.; Liang, T.-M.; Horng, R.-Y.; Chang, M.C.; Ma, C.-C. M. Effects of activated carbon characteristics on the electrosorption capacity of titanium dioxide/activated carbon composite electrode materials prepared by a microwave-assisted ionothermal synthesis method. *J. Colloid Interface Sci.* **2015**, *446*, 352–358.

(26) Liu, P.-I.; Chung, L.-C.; Ho, C.-H.; Shao, H.; Liang, T.-M.; Chang, M.-C.; Ma, C.C. M.; Horng, R.-Y. Comparative insight into the capacitive deionization behavior of the activated carbon electrodes by two electrochemical techniques. *Desalination* **2016**, *379*, 34–41.

(27) Zheng, F.; Li, Y.; Wang, X. Study on effects of applied current and voltage on the ageing of supercapacitors. *Electrochim. Acta* **2018**, *276*, 343–351.

(28) DeRosa, D.; Higashiya, S.; Schulz, A.; Rane-Fondacaro, M.; Haldar, P. High performance spiro ammonium electrolyte for Electric Double Layer Capacitors. *J. Power Sources* **2017**, *360*, 41–47.

(29) Yanchus, D. A.; Kirk, D. W.; Jia, C. Q. Investigating the Effects of Biochar Electrode Macrostructure and Dimension on Electrical Double-Layer Capacitor Performance. *J. Electrochem. Soc.* **2018**, *165*, A305–A313.

(30) Kshetri, T.; Thanh, T. D.; Singh, S. B.; Kim, N. H.; Lee, J. H. Hierarchical material of carbon nanotubes grown on carbon nanofibers for high performance electrochemical capacitor. *Chem. Eng. J.* **2018**, *345*, 39–47.

(31) Lee, E. J.; Nam, I.; Yi, J.; Bang, J. H. Nanoporous hexagonal TiO2 superstructure as a multifunctional material for energy conversion and storage. *J. Mater. Chem. A* **2015**, *3*, 3500–3510.

(32) Sangchoom, W.; Walsh, D. A.; Mokaya, R. Valorization of lignin waste: high electrochemical capacitance of lignin-derived carbons in aqueous and ionic liquid electrolytes. *J. Mater. Chem. A* **2018**, *6*, 18701–18711.

(33) Kasprzak, D.; Stepniak, I.; Galinski, M. Electrodes and hydrogel electrolytes based on cellulose: fabrication and characterization as EDLC components. *J. Solid State Electrochem.* **2018**, *22*, 3035–3047.

(34) Ding, M.; Bannuru, K. K. R.; Wang, Y.; Guo, L.; Baji, A.; Yang, H. Y. Free-Standing Electrodes Derived from Metal-Organic Frameworks/ Nanofibers Hybrids for Membrane Capacitive Deionization. *Adv. Mater. Technol.* **2018**, *3*.

(35) Sriramulu, D.; Yang, H. Y. Free-standing flexible film as a binder-free electrode for an efficient hybrid deionization system. *Nanoscale* **2019**, *11*, 5896–5908.

(36) Cai, W.; Yan, J.; Hussin, T.; Liu, J. Nafion-AC-based asymmetric capacitive deionization. *Electrochim. Acta* **2017**, *225*, 407–415.

(37) Fang, C.-H.; Liu, P.-I.; Chung, L.-C.; Shao, H.; Ho, C.-H.; Chen, R.-S.; Fan, H.-T.; Liang, T.-M.; Chang, M.-C.; Horng, R.-Y. A flexible and hydrophobic polyurethane elastomer used as binder for the activated carbon electrode in capacitive deionization. *Desalination* **2016**, *399*, 34–39.

(38) Hatzell, K. B.; Hatzell, M. C.; Cook, K. M.; Boota, M.; Housel, G. M.; McBride, A.; Kumbur, E. C.; Gogotsi, Y. Effect of Oxidation of Carbon Material on Suspension Electrodes for Flow Electrode Capacitive Deionization. *Environ. Sci. Technol.* **2015**, *49*, 3040–3047.

(39) Qin, M. H.; Deshmukh, A.; Epsztein, R.; Patel, S. K.; Owoseni, O. M.; Walker, W. S.; Elimelech, M. Comparison of energy consumption in desalination by capacitive deionization and reverse osmosis. *Desalination* **2019**, *455*, 100–114.

(40) Ramachandran, A.; Oyarzun, D. I.; Hawks, S. A.; Campbell, P. G.; Stadermann, M.; Santiago, J. G. Comments on "Comparison of energy consumption in desalination by capacitive deionization and reverse osmosis". *Desalination* **2019**, *461*, 30–36.

(41) Qin, M. H.; Deshmukh, A.; Epsztein, R.; Patel, S. K.; Owoseni, O. M.; Walker, W. S.; Elimelech, M. Response to comments on "comparison of energy consumption in desalination by capacitive deionization and reverse osmosis". *Desalination* **2019**, *462*, 48–55.

(42) Patel, S. K.; Qin, M.; Walker, W. S.; Elimelech, M. Energy Efficiency of Electro-Driven Brackish Water Desalination: Electrodialysis Significantly Outperforms Membrane Capacitive Deionization. *Environ Sci Technol* **2020**, 54, 3663-3677.

(43) Portet, C.; Taberna, P.; Simon, P.; Laberty-Robert, C. Modification of Al current collector surface by sol-gel deposit for carbon-carbon supercapacitor applications. *Electrochim. Acta* **2004**, *49*, 905–912.

(44) Kleszyk, P.; Ratajczak, P.; Skowron, P.; Jagiello, J.; Abbas, Q.; Frackowiak, E.; Beguin, F. Carbons with narrow pore size distribution prepared by simultaneous carbonization and self-activation of tobacco stems and their application to supercapacitors. *Carbon* **2015**, *81*, 148–157.

(45) Yang, I.; Kim, S.-G.; Kwon, S. H.; Kim, M.-S.; Jung, J. C. Relationships between pore size and charge transfer resistance of carbon aerogels for organic electric double-layer capacitor electrodes. *Electrochim. Acta* **2017**, *223*, 21–30.

(46) Oz, A.; Gelman, D.; Goren, E.; Shomrat, N.; Baltianski, S.; Tsur, Y. A novel approach for supercapacitors degradation characterization. *J. Power Sources* **2017**, *355*, 74–82.

(47) Berrueta, A.; Ursua, A.; San Martin, I.; Eftekhari, A.; Sanchis, P. Supercapacitors: Electrical Characteristics, Modeling, Applications, and Future Trends. *IEEE Access* **2019**, *7*, 50869–50896.

(48) Qu, Y.; Baumann, T. F.; Santiago, J. G.; Stadermann, M. Characterization of Resistances of a Capacitive Deionization System. *Environ. Sci. Technol.* **2015**, *49*, 9699– 9706.

(49) Gaberscek, M.; Moskon, J.; Erjavec, B.; Dominko, R.; Jamnik, J. The importance of interphase contacts in Li ion electrodes: The meaning of the high-frequency impedance arc. *Electrochem. and Solid State Lett.* **2008**, *11*, A170–A174.

(50) Atebamba, J.-M.; Moskon, J.; Pejovnik, S.; Gaberscek, M. On the Interpretation of Measured Impedance Spectra of Insertion Cathodes for Lithium-Ion Batteries. *J. Electrochem. Sci.* **2010**, *157*, A1218–A1228.

(51) Dykstra, J.; Zhao, R.; Biesheuvel, P.; van der Wal, A. Resistance identification and rational process design in Capacitive Deionization. *Water Res.* **2016**, *88*, 358–370.

(52) Dykstra, J.; Porada, S.; van der Wal, A.; Biesheuvel, P. Energy consumption in capacitive deionization – Constant current versus constant voltage operation. *Water Res.* **2018**, *143*, 367 – 375.

(53) Limpt, B. v. Performance relations in Capacitive Deionization systems. Ph.D. thesis,

Wageningen University, 2010.

(54) Bisquert, J.; Garcia-Belmonte, G.; Fabregat-Santiago, F.; Bueno, P. R. Theoretical models for ac impedance of finite diffusion layers exhibiting low frequency dispersion. *J. Electroanal. Chem.* **1999**, *475*, 152–163.

(55) Bisquert, J.; Compte, A. Theory of the electrochemical impedance of anomalous diffusion. *J. Electroanal. Chem.* **2001**, *499*, 112–120.

(56) Dunn, D.; Newman, J. Predictions of Specific Energies and Specific Powers of Double-Layer Capacitors Using a Simplified Model. *J. Electrochem. Soc.* **2000**, *147*, 820.

(57) Bhat, A. P.; Reale, E. R.; del Cerro, M.; Smith, K. C.; Cusick, R. D. Reducing impedance to ionic flux in capacitive deionization with Bi-tortuous activated carbon electrodes coated with asymmetrically charged polyelectrolytes. *Water Res. X* **2019**, *3*.

(58) Hemmatifar, A.; Stadermann, M.; Santiago, J. G. Two-Dimensional Porous Electrode Model for Capacitive Deionization. *J. Phys. Chem. C* **2015**, *119*, 24681–24694.

(59) Ferguson, T. R.; Bazant, M. Z. Nonequilibrium Thermodynamics of Porous Electrodes. *J. Electrochem. Soc.* **2012**, *159*, A1967–A1985.

(60) High surface area carbon aerogel monoliths with hierarchical porosity. *J. Non. Cryst. Solids* **2008**, *354*, 3513–3515.

(61) Hawks, S. A.; Knipe, J. M.; Campbell, P. G.; Loeb, C. K.; Hubert, M. A.; Santiago, J. G.; Stadermann, M. Quantifying the flow efficiency in constant-current capacitive deionization. *Water Res.* **2018**, *129*, 327–336.

(62) Hawks, S. A.; Ramachandran, A.; Porada, S.; Campbell, P. G.; Suss, M. E.; Biesheuvel, P. M.; Santiago, J. G.; Stadermann, M. Performance metrics for the objective assessment of capacitive deionization systems. *Water Res.* **2019**, *152*, 126–137.

(63) Hawks, S. A.; Ceron, M. R.; Oyarzun, D. I.; Pham, T. A.; Zhan, C.; Loeb, C. K.; Mew, D.; Deinhart, A.; Wood, B. C.; Santiago, J. G. et al. Using Ultramicroporous Carbon for the Selective Removal of Nitrate with Capacitive Deionization. *Environ. Sci. Technol.* **2019**, *53*, 10863–10870.

(64) Oren, Y. Capacitive delonization (CDI) for desalination and water treatment - past, present and future (a review). *Desalination* **2008**, *228*, 10–29.

(65) Gabelich, C. J.; Tran, T. D.; Suffet, I. H. Electrosorption of inorganic salts from aqueous solution using carbon aerogels. *Environmental Science & Technology* **2002**, *36*, 3010–3019.

(66) Jung, H. H.; Hwang, S. W.; Hyun, S. H.; Kang-Ho, L.; Kim, G. T. Capacitive deionization characteristics of nanostructured carbon aerogel electrodes synthesized via ambient drying. *Desalination* **2007**, *216*, 377–385.

(67) Levi, M.; Aurbach, D. Simultaneous measurements and modeling of the electrochemical impedance and the cyclic voltammetric characteristics of graphite electrodes doped with lithium. *J. Phys. Chem. B* **1997**, *101*, 4630–4640.

(68) Newman, J.; Thomas-Alyea, K. E. *Electrochemical Systems*; 2012.

(69) Marcus, Y. THERMODYNAMICS OF SOLVATION OF IONS .5. GIBBS FREEENERGY OF HYDRATION AT 298.15-K. *J. Chem. Soc., Faraday Trans.* **1991**, *87*, 2995–2999.

(70) Qu, Y.; Campbell, P. G.; Hemmatifar, A.; Knipe, J. M.; Loeb, C. K.; Reidy, J. J.; Hubert, M. A.; Stadermann, M.; Santiago, J. G. Charging and Transport Dynamics of a Flow-Through Electrode Capacitive Deionization System. *J. Phys. Chem. B* **2018**,

(71) Ramachandran, A.; Hawks, S. A.; Stadermann, M.; Santiago, J. G. Frequency analysis and resonant operation for efficient capacitive deionization. *Water Research* **2018**, *144*, 581–591.

(72) Ramachandran, A.; Hemmatifar, A.; Hawks, S. A.; Stadermann, M.; Santiago, J. G. Self similarities in desalination dynamics and performance using capacitive deionization. *Water Research* **2018**, *140*, 323–334.

(73) Hemmatifar, A.; Palko, J. W.; Stadermann, M.; Santiago, J. G. Energy breakdown in capacitive deionization. *Water Research* **2016**, *104*, 303–311.

(74) Robinson, D. B. Optimization of power and energy densities in supercapacitors. *Journal of Power Sources* **2010**, *195*, 3748–3756.

(75) Robinson, D. B.; Wu, C.-A. M.; Jacobs, B. W. Effect of Salt Depletion on Charging Dynamics in Nanoporous Electrodes. *Journal of The Electrochemical Society* **2010**, *157*, A912.

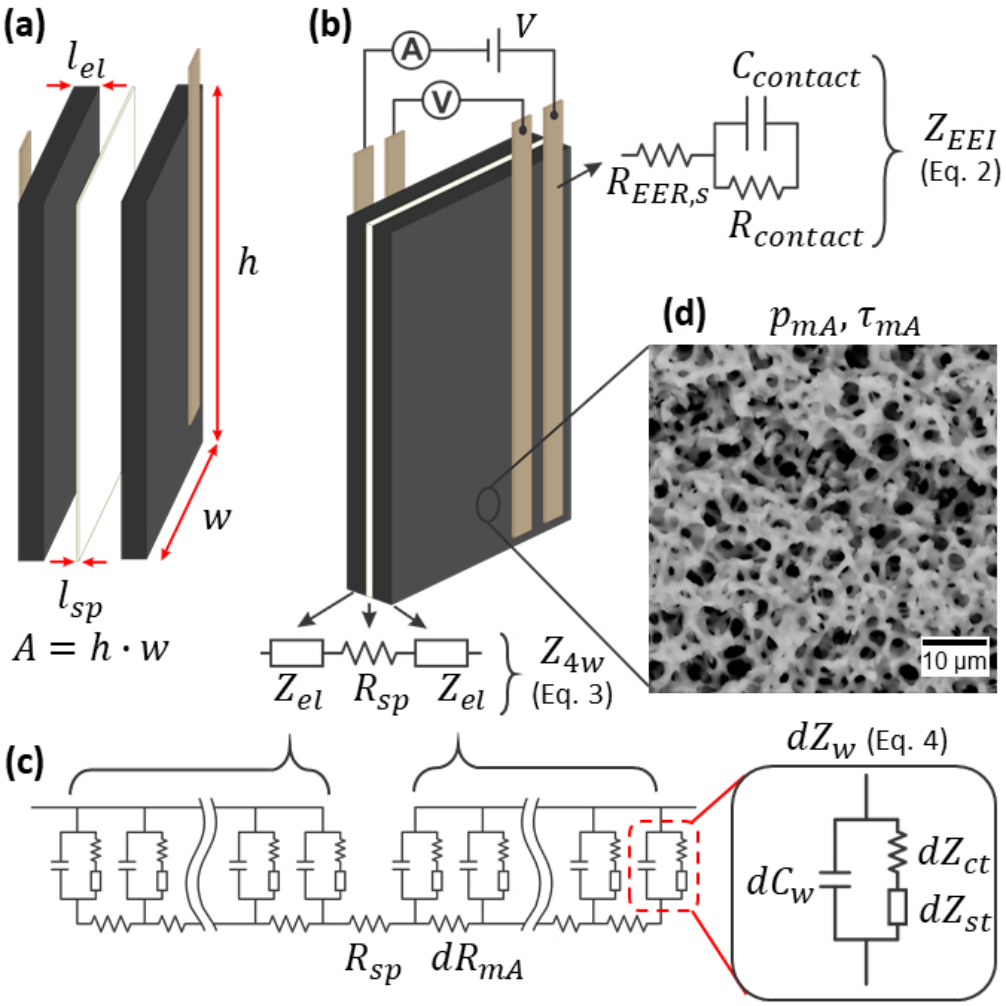
(a)
l_{el}
h
w
l_{sp}
$A = h \cdot w$
(b)
A
V
V
$C_{contact}$
$R_{EER,s}$
$R_{contact}$
Z_{EEI}
(Eq. 2)
Z_{el} R_{sp} Z_{el}
Z_{4w}
(Eq. 3)
(d)
p_{mA}, τ_{mA}
10 µm
(c)
dZ_w (Eq. 4)
dC_w
dZ_{ct}
dZ_{st}
R_{sp} dR_{mA}